Chinese Physics B

Structural evolution and bandgap modification of a robust mixed-valence compound $Eu_9MgS_2B_{20}O_{41}$ under pressure

To cite this article before publication: Boyang Fu *et al* 2025 *Chinese Phys. B* in press https://doi.org/10.1088/1674-1056/add4e1

Structural evolution and bandgap modification of a robust mixed-valence compound $Eu_9MgS_2B_{20}O_{41}$ under pressure

Boyang Fu (符博洋)[1], Wenfeng Zhou (周文风)[2], Fuyang Liu (刘扶阳)[3], Luhong Wang (王鲁红)[4], Haozhe Liu (刘浩哲)[3], Sheng-Ping Guo (郭胜平)[2,†] and Weizhao Cai (蔡伟照)[1,†]

[1]*School of Materials and Energy, University of Electronic Science and Technology of China, Chengdu 611731, China*
[2] *Yunnan Key Laboratory of Electromagnetic Materials and Devices, National Center for International Research on Photoelectric and Energy Materials, School of Material and Energy, Yunnan University, Kunming, Yunnan 650091, China*
[3]*Center for High Pressure Science and Technology Advanced Research, Haidian, Beijing 100094, China*
[4]*Shanghai Advanced Research in Physical Sciences, Shanghai, 201203, China*

The recently discovered mixed-valence compound $Eu_9MgS_2B_{20}O_{41}$, is composed of triple-Kagomé-layers separated by nonmagnetic Mg^{2+} ions, and intervalence charge transfer has been observed in the mixed Eu^{2+} and Eu^{3+} ions within the Kagomé layers, exhibiting similar characteristics typical of a quantum spin liquid. In this study, high-pressure *in situ* X-ray diffraction measurements on $Eu_9MgS_2B_{20}O_{41}$ were conducted within the range of 0.1 MPa to 64.4 GPa. The results revealed that the stabilization of ambient-pressure phase, with no transition from mixed valence to single valence observed within the studied pressure range. The bulk modulus of the sample was determined to be 167.3(28) GPa and 180.8(17) GPa, for the single crystal and powder X-ray diffraction data at room temperature, respectively. These magnitudes correspond to approximately 40% of the bulk modulus of diamond. Moreover, absorption spectroscopy measurements were carried out up to 37.9 GPa, revealing a ~20% reduction in the energy band gap, mainly due to the shortened Eu-O bond lengths. The relationship between pressure and band gap demonstrates a nearly linear trend, with a slope of -0.013 eV/GPa. The findings of the present study imply that the studied sample demonstrates a considerable robustness under extreme pressures.

Keywords: Diamond anvil cells；X-ray diffraction；Crystal structure; High pressure

† Corresponding author. E-mail: spguo@ynu.edu.cn
† Corresponding author. E-mail: wzhcai@uestc.edu.cn

PACS: 07.35.+k; 61.05.cp; 74.62.Bf; 52.77.Fv;

1. Introduction

Materials featuring Kagomé lattice are notable for their geometric frustration and characteristic electronic structures. Such lattice usually correlate to a variety of intriguing quantum states, such as unconventional superconductivity,[1–3] valence fluctuations[4,5] and non-Fermi-liquid state[6,7]. It is generally agreed that the material properties are determined by the four degrees of freedom: lattice, charge, spin, and orbital, and their coupling interactions. When spin is considered as a single degree of freedom, insulating magnetic Kagomé materials have been shown to display excited ground states of magnetism, including the quantum spin liquid (QSL) state, which is a concept within the framework of Anderson's resonating valence bond theory.[8] QSL represents a ground state characterized by significant quantum fluctuations at extremely low temperatures, a phenomenon commonly observed in related quantum spin systems. When the energetics of the spins are suppressed through reducing the temperature, the disordered spin state may either freeze into a spin glass state or an ordered state. The S = 1/2 Kagomé lattice Heisenberg antiferromagnet has been identified as a favorable candidate for exploring QSL materials, owing to the frustration of long-range magnetic order induced by its network of corner-sharing triangles.[9–11] However, the quest for QSL states has thus far proven to be a formidable challenge, with only a few limited systems having been identified as QSL. A notable example is $Cu_3(OH)_6Cl_2$, which has a structure comprising Cu^{2+} ions (d^9, S = 1/2) arranged on a Kagomé lattice.[12] When rare-earth ions are introduced into the triangle of the Kagomé lattice, the formed compounds may possess QSL since they result in the geometrical frustration of antiferromagnetic interactions among neighboring magnetic ions.[13–16]

On the other hand, mounting interest is directed towards the examination of correlation effects and ordering states in partially filled Kagomé lattices, with the prospect of doping inducing unconventional superconductivity.[1,17,18] At van Hove filling, the Fermi surface exhibits a perfect nesting, characterized by saddle points on the Brillouin zone edges.[19] Varying Hubbard U and nearest-neighbor Coulomb V interactions yield a variety of ground states, including ferromagnetism, charge density

wave (CDW) orders, superconductivity, and charge bond.[18,19] High pressure is a clean method that can be used to tune the electronic properties without the introduction of impurities.[20–23] It is commonly used as a control parameter to tune the state of unconventional superconductivity[24,25] and CDW state [26,27]. For instance, in the V-based Kagomé compound KV_3Sb_5, its superconducting transition temperature T_c, which is equal to 0.9 K at ambient pressure, is reported. However, applying a pressure of 0.4 GPa raises the transition temperature to 3.1 K, and the double superconducting dome is observed upon further compression.[28] In another Cr-based Kagomé material $CsCr_3Sb_5$, an increase in pressure leads to the disappearance of initial density-wave orders, and the occurrence of superconductivity at a quantum critical point at approximately 4 GPa.[29]

However, mixed valence materials with Kagomé lattice and CDW feature are rarely reported. As was stated in the previous reports, mixed-valence compounds are generally sensitive to the external conditions (e.g., pressure, magnetic field, and temperature). These conditions ultimately result in the regulation of the valence states of atoms through spin fluctuations. This phenomenon can be interpreted as the quantum merging of two electronic setups, corresponding respectively to the different fillings of n and n-1 in the rare earth 4*f*-shell. In this scenario, an electron has the capability to oscillate between a confined 4*f*-orbital and a more delocalized 5*d*-6*s* state. Experimental evidence for this phenomenon has been predominantly observed in rare earth compounds. For instance, at pressures exceeding 2 GPa, TmTe displays a novel ferromagnetic phase related to its mixed valence state.[30] The valences of both Eu and Yb in $Eu_{0.5}Yb_{0.5}Ga_4$ changes towards a 3+ state as pressure is increased.[31] In the case of the compound $EuFe_2As_2$, it has been demonstrated that long-range Eu magnetic order is exhibited, which rivals with superconductivity and the valence instability of Eu atoms under pressure.[32] In the recently reported mixed-valent Eu^{2+}/Eu^{3+}compound $Eu_4Bi_6Se_{13}$, the structure consists of linear chains of Eu atoms extended along the *b*-axis, the composition of trivalent Eu^{3+} gradually increases with increasing pressure.[33] However, high pressure investigations in mixed valence Eu-based system with Kagomé lattice are rarely reported.

Recently, we successfully synthesized the new compound $Eu_9MgS_2B_{20}O_{41}$, which consists of triple-Kagomé-layer slabs containing mixed-valent Eu^{2+} and Eu^{3+} ions and exhibits spin fluctuations at 16 K.[16] This observation motivates us to further investigate its structural evolution and bandgap changes under compression. Through high-pressure X-ray diffraction measurements, we observed that the material exhibits high structural stability across an extensive pressure range (0-64.4 GPa). Furthermore, the analysis of absorption spectroscopy data revealed a nearly linear decrease in the band gap energy with increasing pressure, which is mainly attributed to the shortening of the Eu-O bond lengths under compression.

2. Experimental Section

2.1. Synthesis of $Eu_9MgS_2B_{20}O_{41}$ single crystals

$Eu_9MgS_2B_{20}O_{41}$ single crystals were synthesized through solid-state reactions at ambient pressure using the flux method, as previously described.[16] The starting materials Eu_2O_3 (99.9%), Mg (99.9%), B (99.9%), S (99.999%), and B_2O_3 (99.9%)—were combined in a molar proportion of 9:2:4:4:18. Potassium iodide (KI) with 99% purity served as the fluxing agent. The mixture was finely ground using an agate mortar, compressed into pellets, and subsequently positioned within quartz tubes. The quartz tubes were depleted of air to attain a vacuum pressure of 1×10^{-4} torr and then securely sealed with a flame, ensuring a stable vacuum condition throughout the synthetic process. The sample was subsequently positioned inside a muffle furnace and subjected to a precise heating schedule. Over a period of 5 hours, the temperature was gradually raised from room temperature to 300 °C, kept at 300 °C for a further 5 hours, then increased gradually to 650 °C over 5 hours, where it was maintained for another 5 hours. Subsequently, the furnace was heated to 950 °C over 5 hours, where the sample was held for 7 days. Finally, the sample was slowly cooled to 300 °C over 5 days. To ensure reproducibility, the synthesis of $Eu_9MgS_2B_{20}O_{41}$ was repeated across five independent batches. Single-crystal XRD analysis confirmed identical lattice parameters (a = 8.2717(9) Å, c = 24.917(5) Å) and mixed-valent Eu^{2+}/Eu^{3+} configurations in all batches, with a yield consistency of ~90%.

2.2. High pressure single crystal X-ray measurements

High pressure *in situ* single crystal X-ray diffraction (SXRD) measurements of $Eu_9MgS_2B_{20}O_{41}$ were conducted using a Bruker D8 Venture single crystal X-ray diffractometer with Helios AgKα radiation (λ = 0.56086 Å). A 70°-opening-angle symmetric diamond anvil cell (DAC) was employed to achieve high pressures reaching up to 37 GPa. Rhenium gaskets were precompressed to 50 μm thick, and subsequently, holes with a diameter of approximately 100 μm were laser drilled to function as the sample chambers. Silicone oil was used as the pressure-transmitting medium (PTM). The ruby fluorescence method was applied for pressure calibration.[34] The initial X-ray data were collected and processed using the APEX5 software. The single-crystal structure was refined using the SHELXL-97 program. The BO_3 and BO_4 units were treated as rigid entities, and their B-O bond lengths were constrained in length, comparable to that at ambient pressure. The lattice parameter V(P) data of $Eu_9MgS_2B_{20}O_{41}$ were subjected to least-squares fitting using the EoSFit7c software, which employed the third-order Birch-Murnaghan equation of state (EoS).[35] The following equation is used to calculate the third-order EoS: $P(V) = 3B_0/2[(V_0/V)^{7/3}–(V_0/V)^{5/3}]\{1+3/4(B_0'–4)[(V_0/V)^{2/3}–1]\}$. In the equation, P indicates the pressure, V_0 is the ambient-pressure volume, V is the high-pressure volume, B_0 is the bulk modulus, and B_0' is the derivative of the bulk modulus with respect to pressure. The variable-pressure crystallographic data, and selected bond lengths are listed in Tables S1 and S2, respectively.

2.3. High pressure synchrotron powder X-ray measurements

The high-pressure synchrotron *in situ* powder X-ray diffraction (PXRD) data were recorded at the beamline 13-BM-C of the Advanced Photon Source (APS), Argonne National Laboratory (ANL). For the X-ray diffraction experiments conducted at APS, a 20 μm diameter of monochromatic X-ray beams and a 0.4143 Å wavelength were employed. The CeO_2 powder was employed as the calibration standard. A powder sample measuring 50 μm × 50 μm × 10 μm, along with a small piece of gold, was loaded into the DAC chamber. The pressure was determined using the equation of state of gold.[36] Silicone oil was used as PTM. The Dioptas program was employed to

integrate the diffraction images.[37] The obtained X-ray diffraction patterns were fitted using the Le Bail method with the aid of GSAS-EXPGUI package.[38] Furthermore, performing least-squares fitting on V(P) data used the 3rd-order Birch-Murnaghan equation of state with the assistance of EoSFit7c software.[35] The initial structure models for refining all powder X-ray data were derived from the single crystal structures.

2.4. High pressure UV-vis absorption measurements

High-pressure *in situ* UV-vis absorption spectroscopy experiments were carried out with a 2-in-1 deuterium-halogen lamp light source, with spectra recorded for 0.75 seconds each, spanning a wavelength range from 300 nm to 900 nm. Prior to the absorption measurements, the spectrometer was calibrated using the absorption edge of a standard sapphire sample to eliminate potential errors. The potential for limitations resulting from scattering losses at elevated pressures is acknowledged, though its impact on the measurements is considered negligible. Silicone oil was used as the PTM and the direct band gap values were obtained by extrapolating the linear portion of the curve plotting $(\alpha hv)^2$ in relation to hv. Here, α denotes the absorption coefficient, h represents the Planck constant, and v stands for the photon frequency.

3. Results and Discussion

3.1. Structural stability of $Eu_9MgS_2B_{20}O_{41}$ at high pressure

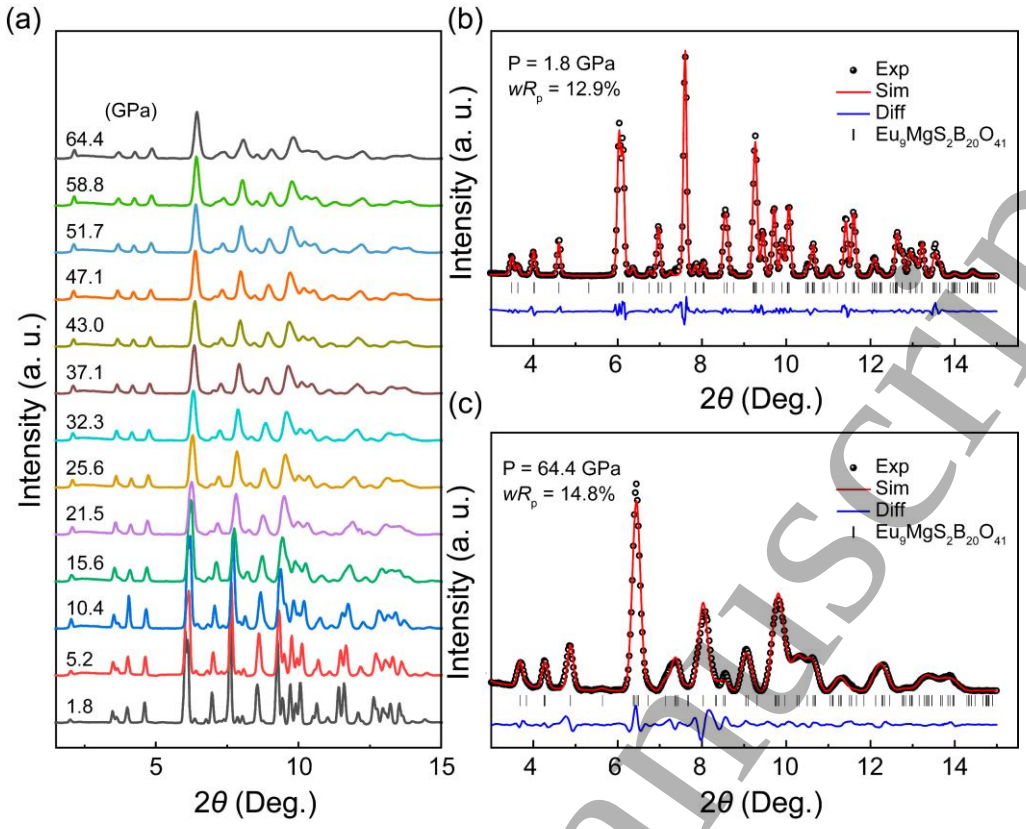

Figure 1. (a) Representative XRD patterns of $Eu_9MgS_2B_{20}O_{41}$ powder under high pressures. Le Bail fits of X-ray data at (b) 1.8 and (c) 64.4 GPa. The measured scattering intensity is depicted by the black circles, while the red solid line denotes the fitted curve corresponding to the data. The Bragg reflection points of the sample are indicated at the bottom by vertical bars (black lines).

In order to ascertain the structural stability of $Eu_9MgS_2B_{20}O_{41}$ under compression, synchrotron powder X-ray diffraction (PXRD) was performed up to an applied pressure of 64.4 GPa at room temperature. At ambient conditions, $Eu_9MgS_2B_{20}O_{41}$ crystallizes in the hexagonal $P6_3/m$ symmetry ($Z = 2$), with lattice parameters $a = b = 8.2717(9)$ Å, $c = 24.917(5)$ Å and $V = 1476.4(4)$ Å^3. As demonstrated in Figure 1a, there is an absence of a structural phase transition over the pressure range of 0-64.4 GPa. Borates compounds containing BO_3 and BO_4 groups are generally more difficult to undergo structural phase transitions due to the strong rigidity of the BO_3 and BO_4 groups. For example, the YBO_3 and $GdBO_3$ samples did not demonstrate any phase transition within the 40 GPa range.[39] It is evident that all diffraction peaks shift to higher 2θ angle ranges (*i.e.*, smaller *d*-spacing) with increasing the pressure. Concurrently, diffraction peaks became broader, a feature most likely attributable to the quasi-hydrostatic environment created by silicone oil (see Figure S1). The Le Bail method

has been shown to effectively fit the powder diffraction patterns with the ambient pressure phase, yielding lattice parameter at 64.4 GPa:

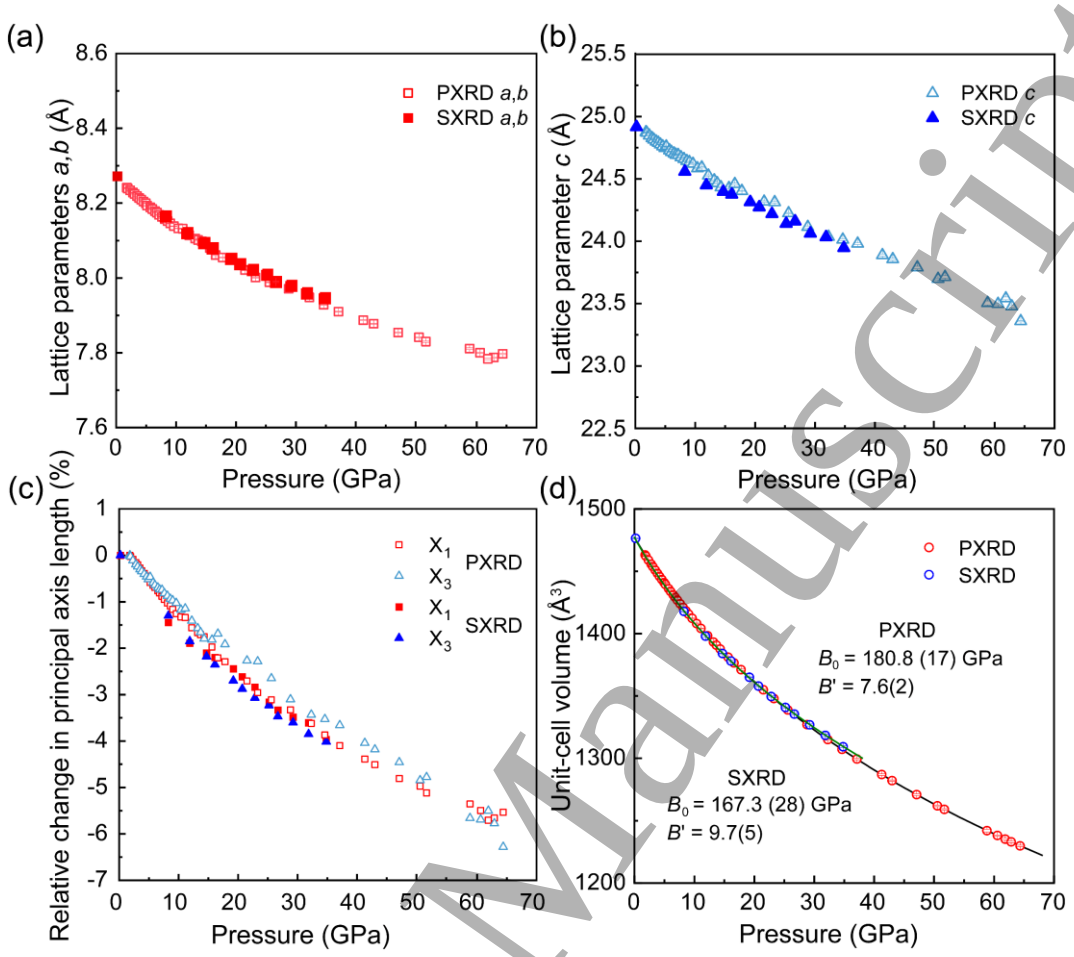

Figure 2. The lattice parameters (a) *a*, *b* and (b) *c* axis from single crystal and powder data of $Eu_9MgS_2B_{20}O_{41}$ under pressure. (c) Relative changes in principal axis length of the sample as changes of pressure. (d) The third-order Birch-Murnaghan equation of state fit to the unit-cell volume data.

a = *b* = 7.7970(18) Å, *c* = 23.359 (6) Å and *V* = 1229.8(6) Å^3. Moreover, SXRD measurements were carried out from ambient to 36.9 GPa to precisely determine the bond changes within the crystal structure under compression. The obtained lattice parameters are well consistent with the PXRD data (Figure 2). As shown in Figure 2a, the lattice parameters exhibit weak anisotropic compression. Specifically, the *c*-axis, which is perpendicular to the densely packed Kagomé layers, demonstrates the most compressibility (Figure 3c). PXRD analysis reveals a strain tensor, designated as K_1, with a magnitude of 1.31(1) TPa^{-1} (the tensor has an orientation angle of 53.8° relative to the *a*-axis). Furthermore, the magnitude of K_1 along this orientation is 1.3 times larger

than that observed along the *c*-axis (where K_c = 1.07(2) TPa^{-1}, see Table S3). This magnitude of linear compressibility is smaller than typical crystalline materials (5-20 TPa^{-1}). For example, the calculated values of the strain tensor for cubic EuS[39] and orthorhombic $LaPO_4$[40] were determined to be 10.2(5) TPa^{-1} and 7.4(6) TPa^{-1} (*c* axis), respectively. It has been demonstrated that the presence of the BO_3 and BO_4 groups results in a substantial increase in the rigidity and incompressibility of the material structure. Such an unusual property allows the sample to possess potential applications in precise microdevices, telecommunication optical fibers in deep sea environments. As shown in Figure 2(d), the unit-cell volume continuously reduces and there is no volume collapse emerged as the pressure increases, suggesting the absence of a structural phase transition. The experimental *V*(P) data from SXRD were well fitted to a the third-order Birch-Murnaghan equation of state (EoS), yielding the zero-pressure bulk modulus B_0 = 167.3(28) GPa and its pressure derivative B' = 9.7(5). The magnitude is slightly smaller than that obtained from PXRD measurements (B_0 = 180.8 (17) GPa and B' = 7.6 (2)). The bulk modulus reveals that the material is extremely hard and is comparable to the reported borates containing flat BO_3 or tetrahedral BO_4 groups. For example, $GdBO_3$ (B_0 = 170(13) GPa) [42] and YBO_3 (B_0 = 164(8) GPa)[43]. The magnitude of the bulk modulus, which is equivalent to 40% that of diamond, signifying the sample's considerable hardness.

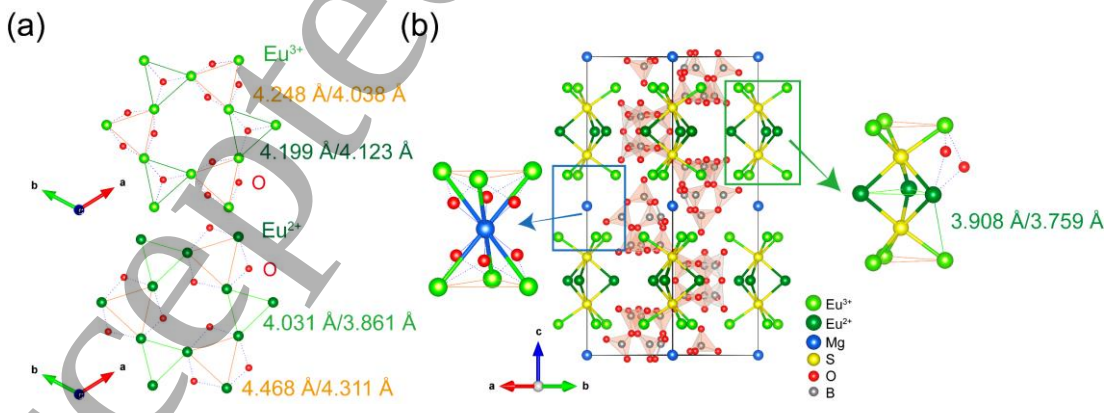

Figure 3. (a) Distorted Kagomé layer of the Eu^{3+} and Eu^{2+} ions viewed along the *c* axis at 0.1 MPa and 36.9 GPa. (b) Cystal structure of $Eu_9MgS_2B_{20}O_{41}$ at ambient pressure and 36.9 GPa. The right inset shows the structure of a triple-Kagomé-layer slab, which three Eu^{3+} ions arranged as triangles

at the top, three Eu^{2+} arranged as triangles in the middle and three Eu^{3+} arranged as triangles at the bottom. The left inset shows positioning of a Mg^{2+} ion between two triple-Kagomé-layer slabs.

For the ambient-pressure phase, the asymmetric unit consists of two Eu, one Mg, one S, four B, and eight O atoms. The three-dimensional (3-D) structure of $Eu_9MgS_2B_{20}O_{41}$ is composed of triple-Kagomé-layer slabs, with the presence of two types of Eu atoms of Eu^{3+} and Eu^{2+}. The distorted Kagomé layer is formed by each Eu atom, as depicted in Figures 1a and 1b. Specifically, the Kagomé layers composed of Eu^{2+} ions are sandwiched between two Kagomé layers consisting of Eu^{3+} ions, resulting in the formation of a triple Kagomé-layer slab. In one unit-cell, two such slabs are presented, and they are separated by nonmagnetic Mg^{2+} ions and BO_3 and BO_4 groups. As shown in Figure 3a, the shortest Eu^{3+}-Eu^{2+} interlayer distance within the triple-Kagomé-layer slab is approximately 3.908 Å at ambient pressure, which is smaller than the intra-layer Eu^{3+}-Eu^{3+} distance (~4.248 Å) or Eu^{2+}-Eu^{2+} (~4.031 Å) distances. However, with an increase in pressure to 36.9 GPa, the shortest Eu^{3+}-Eu^{2+} interlayer distance decreases to 3.759 Å, the intra-layer Eu^{3+}-Eu^{3+} distance reduces to 4.038 Å, and the Eu^{2+}-Eu^{2+} distance shortens to 3.861 Å, respectively. Table S2 illustrates the coordination environments of Eu^{3+} and Eu^{2+} atoms. As BO_3 and BO_4 are rigid units within the structure, the B-O lengths remain largely unchanged across the entire pressure range. The Eu^{3+}-S and the Eu^{2+}-S bonds are formed by S atoms that bridge two Kagomé layers (see Figure 4a). The bond lengths of Eu^{2+}-S/Eu^{3+}-S are 3.048/2.969 Å and decrease to 2.900/2.870 Å at 36.9 GPa. The coordination number of Eu^{3+} cations is eight, with eight O atoms (O2, O3, $O3^{iv}$, O4, O5, O6, O7 and O8, see Figure 4b). It is evident that all Eu^{3+}-O bond lengths undergo slight reductions under compression. In the case of Eu^{2+} cation, the neighboring O atoms are reduced to six (O1, $O1^{iv}$, two O6 atoms, two O7 atoms), and these bonds also are shortened gradually as pressure increases.

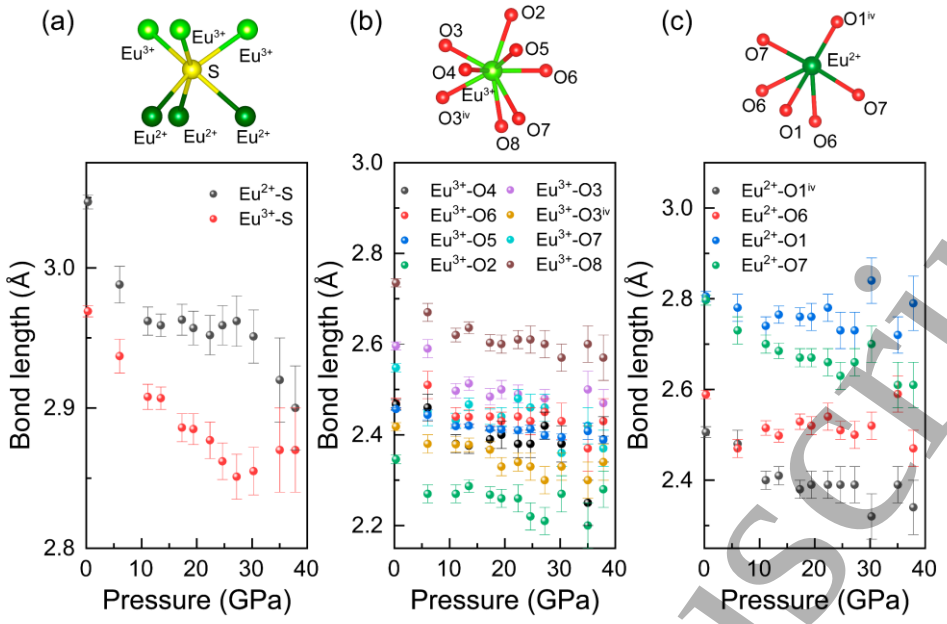

Figure 4. (a) Evolution of Eu^{3+}-S and Eu^{2+}-S bond lengths under pressure. Changes of (b) Eu^{3+}-O and (c) Eu^{2+}-O bond lengths in response to pressure.

3.2. Optical property of $Eu_9MgS_2B_{20}O_{41}$ under high pressure

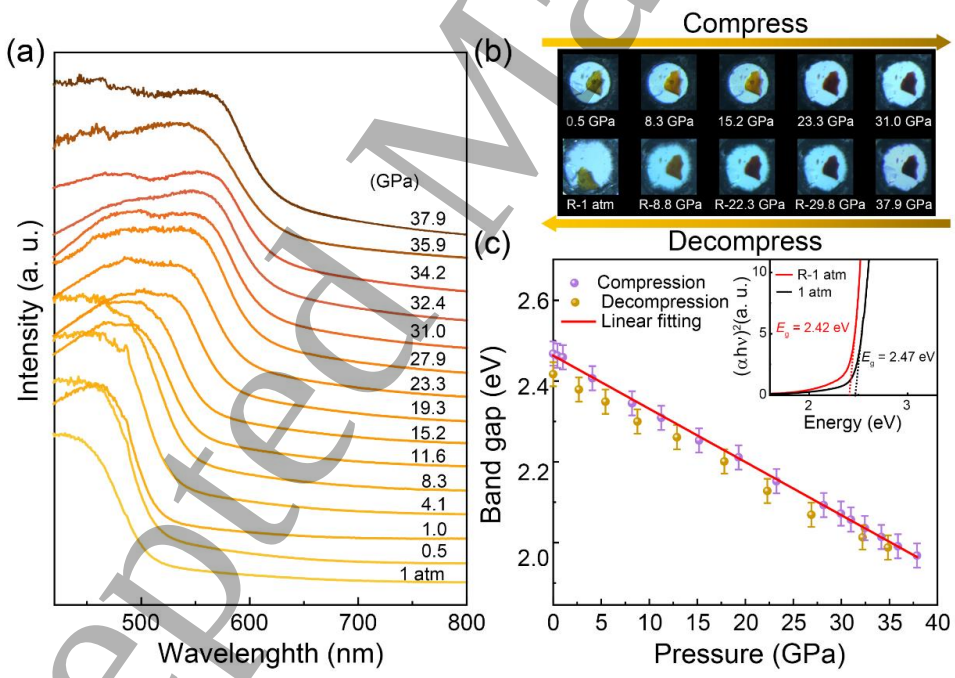

Figure 5. (a) UV-vis optical absorption spectra of $Eu_9MgS_2B_{20}O_{41}$ under compression. (b) Optical images of the sample under compression. (c) Optical bandgap of $Eu_9MgS_2B_{20}O_{41}$ upon increasing and decreasing pressure. The red line implies the results of linear fitting of high-pressure experimental data. The inset shows Tauc plots of the absorption spectra and the bandgaps of $Eu_9MgS_2B_{20}O_{41}$ at ambient and release to the ambient pressure.

High-pressure *in situ* UV-vis absorption measurements were carried out up to 37.9 GPa to investigate the band gap variations under compression. At ambient conditions, $Eu_9MgS_2B_{20}O_{41}$ was identified as a wide band gap semiconductor, exhibiting a direct energy band gap of 2.47 eV at ambient pressure.[16] When the sample was compressed in the silicone oil, the initial light brown color of the sample gradually darkened and changed to almost opaque at a pressure of 37.9 GPa (see Figure 5). Concurrently, the absorption edge undergoes a gradual red-shift, and the band gap reduced to 1.96 eV at 37.9 GPa. According to the density of states (DOS) calculations, we find that the energy gap is primarily attributed to the reduction in Eu–O bond lengths, whereas the Eu–S bond plays a minor role (see Figure S2). As the pressure increases, the Eu–O bond distances undergo a gradual shortening, leading to an enhancement in orbital overlap and, consequently, a reduction in the band gap. The energy band gap, as determined by the slope of the fitted line, exhibits a linear relationship with a slope of -0.013 eV/GPa, which is significantly smaller than the values observed in other sulfide compounds (Figure 5c). For instance, the rate of EuS is 0.089 eV/GPa and the rate of $AgSbS_3$ is 0.066 eV/GPa.[44,45] This finding indicates that the influence of pressure on alterations in the band gap is also very weak, suggesting the robustness of the electronic structures of the sample. Upon extending our linear fitting analysis, we found that the closure of bandgap in the sample occurs at ~190 GPa. It should be noted that this conclusion is reached without consideration of any potential phase transitions. During the decompression process, it was observed that the color changes were reversible, with the color returning to its initial light brown state, implying that the optical bandgap undergoes a reversible modification when subjected to high pressure. These findings are in alignment with the previously discussed XRD measurements. Additionally, high-pressure electrical transport measurements were conducted on the powder sample; however, the recorded electrical resistance values consistently fell outside the designated range when the sample was compressed to 20.3 GPa (see Figure S3).

4. Conclusion

In summary, the crystal structures, and optical properties of $Eu_9MgS_2B_{20}O_{41}$ under

compression have been systematically explored through the utilization of *in situ* single-crystal XRD, powder XRD, and UV-vis optical absorption spectroscopy. The results exhibit that the ambient-pressure hexagonal crystal structure of $Eu_9MgS_2B_{20}O_{41}$ remains stable with pressure increases to 64.4 GPa, suggesting the intriguing hardness and structural stability under high pressure conditions. As the pressure increases, the Eu-S/Eu-O bonds shorten gradually, resulting in a gradual reduction in the optical band gap. The linear slope of the band gap under pressure indicates that the metallization may occur at ~190 GPa, without consideration of the any phase transitions. The structural stability and reversibility of optical bandgap changes exhibited by this compound at high pressures make the material an excellent candidate for a variety of potential applications. These include precision microdevices, deep-sea optical communication fibers, and sensors for high-pressure environments. The integration of such devices into optical communication systems has the potential to enhance the stability and efficiency of signal transmission. Additionally, these devices could facilitate the monitoring and measurement of pressure changes in extreme conditions.

Data availability statement

The data supporting this article have been included as part of the Supplementary Information file.

Acknowledgment

We acknowledge the financial support from the National Natural Science Foundation of China (No. 12274062 and 22371246). Part of this work was carried out at the Synergetic Extreme Condition User Facility (SECUF).

References

[1] Anderson P W 1987 *Science* **235** 1196
[2] Guguchia Z, Khasanov R and Luetkens H 2023 *npj Quantum Mater.* **8** 41
[3] Li Q, Wu Y, Fan X, Zhang Y-J, Zhu X, Zhu Z, Li Y and Wen H-H 2022 *Phys. Rev. B* **106** 214501
[4] Pollmann F, Roychowdhury K, Hotta C and Penc K 2014 *Phys. Rev. B* **90** 035118
[5] Jiang Y-X, Shao S, Xia W, Denner M M, Ingham J, Hossain M S, Qiu Q, Zheng X, Chen H, Cheng Z-J, Yang X P, Kim B, Yin J-X, Zhang S, Litskevich M, Zhang Q,

Cochran T A, Peng Y, Chang G, Guo Y, Thomale R, Neupert T and Hasan M Z 2024 *Nat. Mater.* **23** 1214
[6] Mazin I I, Jeschke H O, Lechermann F, Lee H, Fink M, Thomale R and Valentí R 2014 *Nat. Commun.* **5** 4261
[7] Bauer B, Keller B P, Trebst S and Ludwig A W W 2019 *Phys. Rev. B* **99** 035155
[8] Anderson P W 1973 *Mater. Res. Bull.* **8** 153
[9] Sachdev S 1992 *Phys. Rev. B* **45** 12377
[10] Elser V 1989 *Phys. Rev. Lett.* **62** 2405
[11] Lecheminant P, Bernu B, Lhuillier C, Pierre L and Sindzingre P 1997 *Phys. Rev. B* **56** 2521
[12] Helton J S, Matan K, Shores M P, Nytko E A, Bartlett B M, Yoshida Y, Takano Y, Suslov A, Qiu Y, Chung J-H, Nocera D G and Lee Y S 2007 *Phys. Rev. Lett.* **98** 107204
[13] Harris M J, Bramwell S T, McMorrow D F, Zeiske T and Godfrey K W 1997 *Phys. Rev. Lett.* **79** 2554
[14] Bramwell S T and Gingras M J P 2001 *Science* **294** 1495
[15] Ramirez A P, Hayashi A, Cava R J, Siddharthan R and Shastry B S 1999 *Nature* **399** 333
[16] Chi Y, Xu J, Xue H-G, Zhang Y, Chen X, Whangbo M-H, Guo S-P and Deng S 2019 *J. Am. Chem. Soc.* **141** 9533
[17] Balents L 2010 *Nature* **464** 199
[18] Kiesel M L, Platt C and Thomale R 2013 *Phys. Rev. Lett.* **110** 126405
[19] Wang W-S, Li Z-Z, Xiang Y-Y and Wang Q-H 2013 *Phys. Rev. B* **87** 115135
[20] Gao Y, Liu C, Tian C, Zhu C, Huang X and Cui T 2024 *Chinese Phys. B* **33** 126104
[21] Zhang M-G, Chen L, Feng L, Tuo H-H, Zhang Y, Wei Q and Li P-F 2023 *Chinese Phys. B* **32** 086101
[22] Chen J, Lv X, Li S, Dan Y, Huang Y and Cui T 2024 *Chinese Phys. B* **33** 067104
[23] Cai W, He J, Li H, Zhang R, Zhang D, Chung D Y, Bhowmick T, Wolverton C, Kanatzidis M G and Deemyad S 2021 *Nat. Commun.* **12** 1509
[24] Ortiz B R, Teicher S M L, Hu Y, Zuo J L, Sarte P M, Schueller E C, Abeykoon A M M, Krogstad M J, Rosenkranz S, Osborn R, Seshadri R, Balents L, He J and Wilson S D 2020 *Phys. Rev. Lett.* **125** 247002
[25] Ortiz B R, Sarte P M, Kenney E M, Graf M J, Teicher S M L, Seshadri R and Wilson S D 2021 *Phys. Rev. Materials* **5** 034801
[26] Ortiz B R, Gomes L C, Morey J R, Winiarski M, Bordelon M, Mangum J S, Oswald I W H, Rodriguez-Rivera J A, Neilson J R, Wilson S D, Ertekin E, McQueen T M and Toberer E S 2019 *Phys. Rev. Materials* **3** 094407
[27] Jiang Y-X, Yin J-X, Denner M M, Shumiya N, Ortiz B R, Xu G, Guguchia Z, He J, Hossain M S, Liu X, Ruff J, Kautzsch L, Zhang S S, Chang G, Belopolski I, Zhang Q, Cochran T A, Multer D, Litskevich M, Cheng Z-J, Yang X P, Wang Z, Thomale R, Neupert T, Wilson S D and Hasan M Z 2021 *Nat. Mater.* **20** 1353
[28] Du F, Luo S, Ortiz B R, Chen Y, Duan W, Zhang D, Lu X, Wilson S D, Song Y and Yuan H 2021 *Phys. Rev. B* **103** L220504
[29] Liu Y, Liu Z-Y, Bao J-K, Yang P-T, Ji L-W, Wu S-Q, Shen Q-X, Luo J, Yang J,

Liu J-Y, Xu C-C, Yang W-Z, Chai W-L, Lu J-Y, Liu C-C, Wang B-S, Jiang H, Tao Q, Ren Z, Xu X-F, Cao C, Xu Z-A, Zhou R, Cheng J-G and Cao G-H 2024 *Nature* **632** 1032

[30] Link P, Goncharenko I N, Mignot J M, Matsumura T and Suzuki T 1998 *Phys. Rev. Lett.* **80** 173

[31] Loula G D, Dos Reis R D, Haskel D, Garcia F, Souza-Neto N M and Gandra F C G 2012 *Phys. Rev. B* **85** 245128

[32] Matsubayashi K, Munakata K, Katayama N, Isobe M, Ohgushi K, Ueda Y, Kawamura N, Mizumaki M, Ishimatsu N, Hedo M, Umehara I and Uwatoko Y 2011 *Phys. Rev. B* **84** 024502

[33] Xu M, Jose G C, Cheng M, Peng C, Gonzalez Jimenez J L, Bi W, Li M and Xie W 2025 *J. Phys. Chem. A* **129** 2371

[34] Mao H K, Xu J, and Bell P M 1986 *J. Geophys. Res.* **91** 4673

[35] Angel R J, Alvaro M and Gonzalez-Platas J 2014 *Z. Kristallogr. Cryst. Mater.* **229** 405

[36] Heinz D L and Jeanloz R 1984 *J. Appl. Phys.* **55** 885

[37] Prescher C and Prakapenka V B 2015 *High Pressure Res.* **35** 223

[38] Toby B H 2001 *J. Appl. Crystallogr.* **34**210

[39] Wang P, He D, Xu C, Ren X, Lei L, Wang S, Peng F, Yan X, Liu D, Wang Q, Xiong L and Liu J 2014 *J. Appl. Phys.* **115** 043507

[40] Singh D, Rajagopalan M, Husain M and Bandyopadhyay A K 2000 *Solid State Commun.* **115** 323

[41] Lacomba-Perales R, Errandonea D, Meng Y and Bettinelli M 2010 *Phys. Rev. B* **81** 064113

[42] Turnbull R, Errandonea D, Sans J Á, Cuenca-Gotor V P, Vilaplana R I, Ibáñez J, Popescu C, Szczeszak A, Lis S and Manjón F J 2021 *J. Alloys Compd.* **866** 158962

[43] Turnbull R, Errandonea D, Cuenca-Gotor V P, Sans J Á, Gomis O, Gonzalez A, Rodríguez-Hernandez P, Popescu C, Bettinelli M, Mishra K K and Manjón F J 2021 *J. Alloys Compd.* **850** 156562

[44] Monteseguro V, Barreda-Argüeso J A, Ruiz-Fuertes J, Rosa A D, Meyerheim H L, Irifune T and Rodriguez F 2022 *Sci. Rep.* **12** 1217

[45] Qin T, Wu M, Wang K, Wu Y and Huang H 2024 *Chinese Phys. B* **33** 118101